Introduction

This supporting information provides figures related to the choice of pre-processing regime applied to our noise recording prior to the calculation of the cross correlation functions (Figs. S1 and S2). We show examples of the group velocity - period diagrams used when creating the phase velocity data set (Fig. S3). We also include a figure illustrating our choice of damping parameter in the Rayleigh and Love wave phase velocity inversions (Fig. S4). Fig. S5 and S6 show the data misfit information for our phase velocity tomography. Figs. S8 - S15 provide information on the vertical and horizontal resolution of of our phase velocity tomography through sensitivity kernels and checkerboard tests. Fig. S16 shows the azimuthal variation of our Love wave phase velocities.

Text S1. Effect of noise pre-processing on the signal-to-noise ratio of the cross-correlation functions

Fig. S1 shows the evolution of the signal-to-noise ratio of the cross correlation functions as a function of the amount of data stacked. The signal-to-noise ratio is defined as the ratio between the amplitude of the surface wave arrival, and a 20 s long window of coda energy that arrives late in the correlation function. We show examples for four different noise pre-processing schemes. We test the effects of the noise window duration (1-hour or 4-hours long), as well as different forms of amplitude normalization (1-bit normalization or amplitude clipping). It is clear that the choice of noise pre-processing has little effect on the final signal-to-noise ratios. All pre-processing approaches result in an average signal-to-noise ratio of $\sim$ 16 once all data have been stacked. This analysis was performed on a subset of the data that spanned a period of 3-months. The final tomography utilized data from the full 16-month long deployment of the DANA network.

Text S2. Effect of noise pre-processing on the coherency of the cross-correlation functions.

Fig. S2 shows the power spectral densities of the cross correlation functions under the four different processing schemes (Text S1.). As with signal-to-noise ratio, there is little variation in coherency between the different approaches. However, amplitude clipping does appear to have a slightly higher power spectral density than the 1-bit normalization approach. The 4-hour long windows are also slightly more coherent than the 1-hour long windows. Given this, we choose the pre-processing scheme that implements amplitude clipping on noise windows that are 4-hours long.

Text S3. Examples of group velocity-period diagrams.

Fig. S3 shows four examples of group velocity - period diagrams that were used in the study. We show examples of Rayleigh wave diagrams taken from the radial-radial cross-correlation functions between stations with inter-station distances of 17 km and 61 km. We also show transverse-transverse cross-correlation functions taken for stations separated by 22 km and 65 km. On the 17 km distance RR component, group and phase velocity values are not picked for periods longer than 4.0 s, as the measurements at long periods are deemed to be unreliable due to the wavelength criterion. On the 22 km TT component, velocity values are not picked above 5.0 s period for the same reason. The group velocity values begin to increase rapidly up to unrealistic values for periods greater than these cut-offs.

Text S4. Effect of damping on the phase velocity inversion.

Fig. S4 shows model variance vs. RMS travel time residual as a function of damping parameter for the final models produced by the Rayleigh and Love wave phase velocity inversions at 4.0 s period. We select, through subjective judgement, the level of damping that gives us a substantial decrease in model variance for only a modest increase in data misfit. We trialled damping parameters with a range between $\epsilon = 0$ and $\epsilon = 500$.

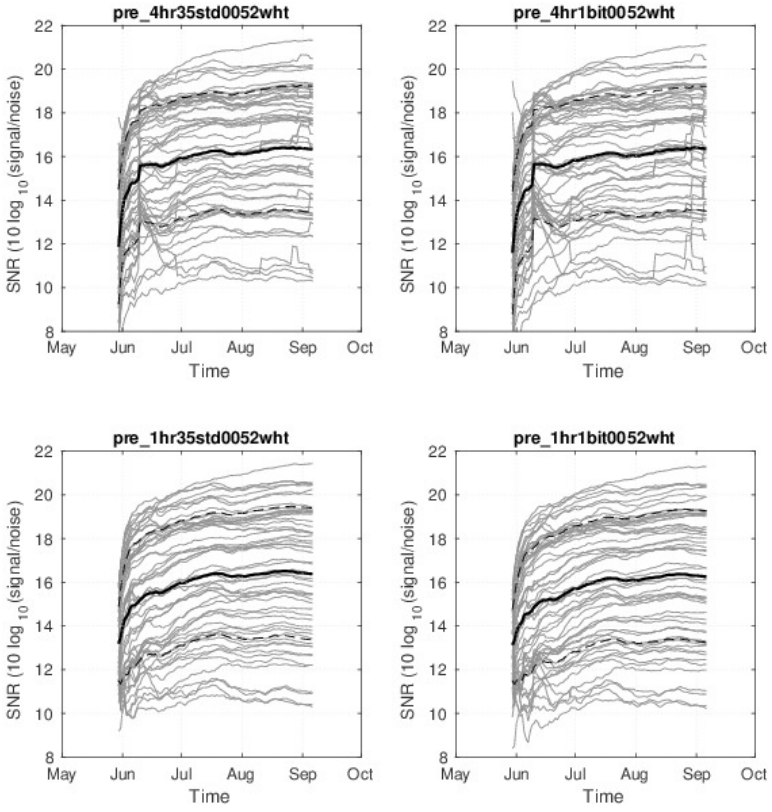

Figure S1. Effect of noise pre-processing on the signal-to-noise ratio of the cross correlation functions as a function of the amount of data stacked. Each panel shows a different pre-processing scheme. Top left: 4-hour long noise windows with amplitude clipping. Top right: 4-hour long noise windows with 1-bit normalization. Bottom left: 1-hour long noise window with amplitude clipping. Bottom right: 1-hour long noise window with 1-bit normalization. Grey lines represent individual cross correlation functions, and the solid black line represents the mean of all correlation functions. The dashed blacked line indicates one standard deviation.

Text S5. Data misfit to the Rayleigh and Love wave phase velocity tomography.

Figs. S5 and S6 show the data misfit of the phase velocity tomography for Rayleigh and Love waves, respectively. We show the misfit of the initial, constant velocity model prior to the tomographic inversion, and the data misfit of the final phase velocity model at 2.0, 4.0, 6.0 and 8.0 s period. The final phase velocity models are shown in Fig. 3 and 4 in the main text.

Text S6. Data misfit of the S-wave velocity inversion.

Fig. S7 shows the fit of the individual phase velocity dispersion curves at three nodes in the S-wave velocity model (Fig. 5 in the main text). We show the dispersion curves that are extracted from the phase velocity tomographies for both Rayleigh and Love waves, and the corresponding dispersion curves predicted by our final S-wave velocity model. The improvement of fit provided by the linearised inversion over the neighbourhood algorithm result is shown in each row.

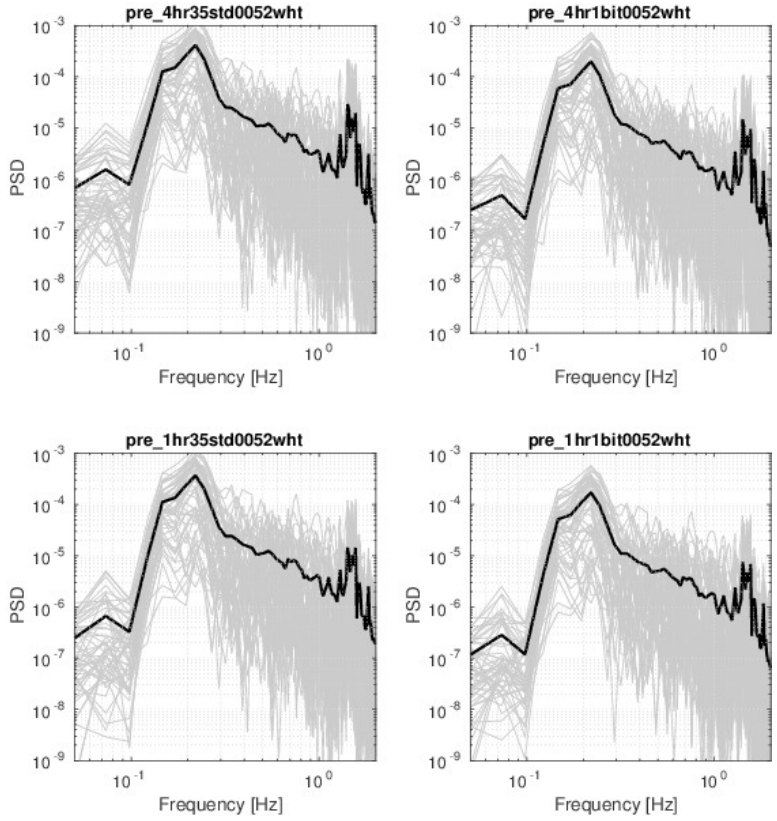

Figure S2. Effect of noise pre-processing on the coherency of the cross correlation functions. Each panel shows a different pre-processing scheme. Top left: 4-hour long noise windows with amplitude clipping. Top right: 4-hour long noise windows with 1-bit normalization. Bottom left: 1-hour long noise window with amplitude clipping. Bottom right: 1-hour long noise window with 1-bit normalization. Grey lines represent individual cross correlation functions, and the solid black line represents the mean of all correlation functions.

Text S7. Rayleigh and Love wave sensitivity kernels.

Fig. S8 shows the partial derivatives of phase velocity with respect to S-wave velocity as a function of depth at each grid point is our final isotropic S-wave velocity model. We show period of 2.0 s, 5.0 s and 8.0 s. This illustrates the depth sensitivity of our phase velocity observations and constrains the depth resolution of our S-wave velocity model. Our long period Rayleigh wave observations maintain sensitivity up to 10.0 km depth, whilst our Love wave observations are sensitive to more shallow structure, mostly above 5.0 km depth.

Text S8. Depth resolution of the S-wave velocity model

Fig. S9 shows the final resolution kernels of the S-wave velocity model, after the linearised inversion. It is clear that the structure closest to the surface is best resolved by the data set, which is to be expected for surface wave studies, where resolution at depth depends on observations from longer period waves. This effect is most obvious within the Istanbul zone, where the pervasive low S-wave velocities near the surface caused by the presence of sedimentary basins results in relatively lower resolution below $\sim$ 3 km depth.

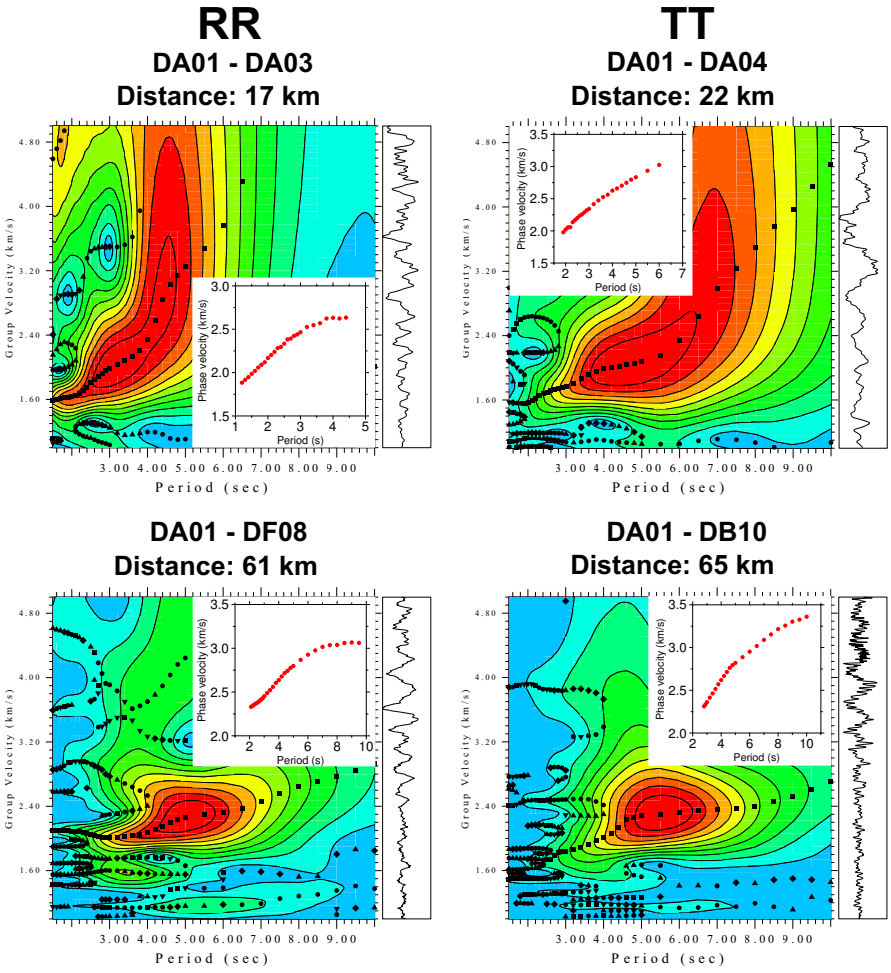

Figure S3. Examples of period - group velocity maps for four inter-station pairs. The inset dispersion curves are the corresponding phase velocity curves that were picked, shown in red dots. Red colours indicate a larger amplitude for the envelope of the wave at the given period, for each velocity. The black squares indicate the likely group velocity values, which are picked manually. We show dispersion maps for both short and long distances ($<$ 25 km and $>$ 60 km) for both Rayleigh (left column) and Love (right column) waves. The bars of the right hand side of each period - group velocity map shows the cross correlation function.

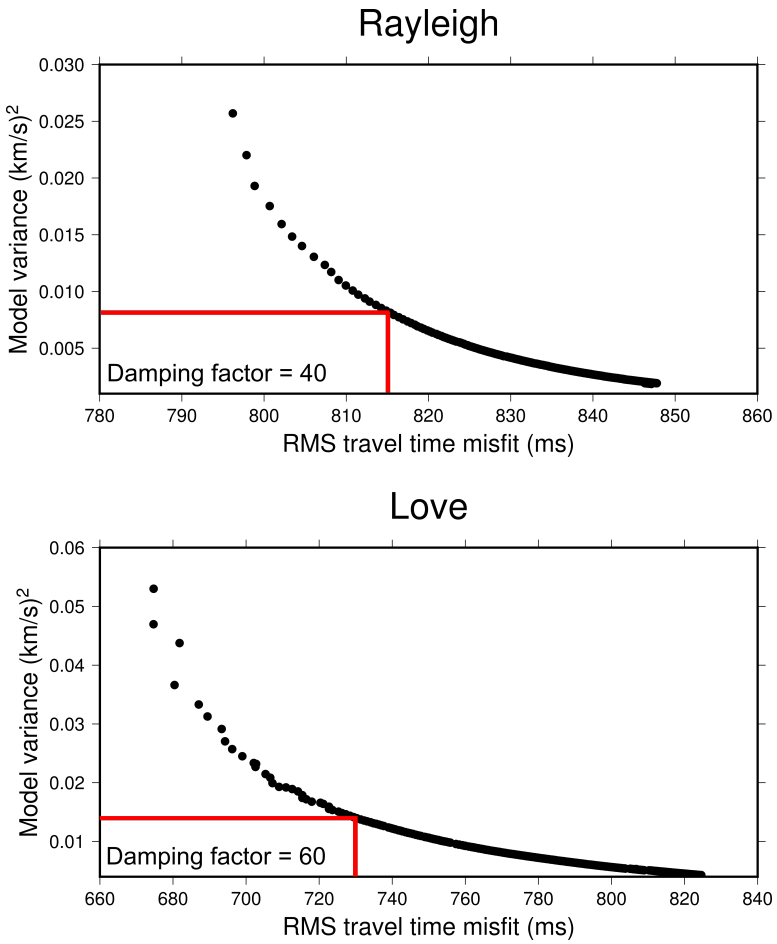

Figure S4. Top: Effect of damping on the Rayleigh wave phase velocity inversion at 4.0 s period. Bottom: Effect of damping on the Love wave phase velocity inversion. Each black dot represents a trial of a different damping parameter between 0 and 500. The red lines indicate the model variance and data misfit of the chosen damping factor for the inversion, which is indicated on each figure.

Text S9. Checkerboard tests for the Rayleigh and Love wave phase velocity.

Fig. S10 shows checkerboard tests that illustrate the horizontal resolution of the Rayleigh wave phase velocity tomography between 3.0 and 9.0 s, Fig. S11 shows the same image for the Love wave tomography. The maps were obtained by inverting for the original checkerboard pattern from a constant velocity starting model using a noisy synthetic data set with the same ray path distribution as our tomography. The standard deviation of the white noise added to the input travel times is 1.5 s. We maintain good horizontal resolution at all periods, though there is some smearing at long periods (9.0 s) for both Rayleigh and Love waves. In general, the checkerboard pattern is recovered better using the ray distribution of the Love wave tomography, rather than the Rayleigh wave tomography. The corresponding ray path distributions are shown in Figs. S14 and S15. In order to test the robustness of our phase velocity inversion against anomalies of different shapes and wavelengths, we also include tests to recover a velocity model consisting of spikes (Fig. S12) and a randomly generated velocity model (Fig. S13). Both of these tests were carried out on the Rayleigh wave ray path distribution at 4 s period.

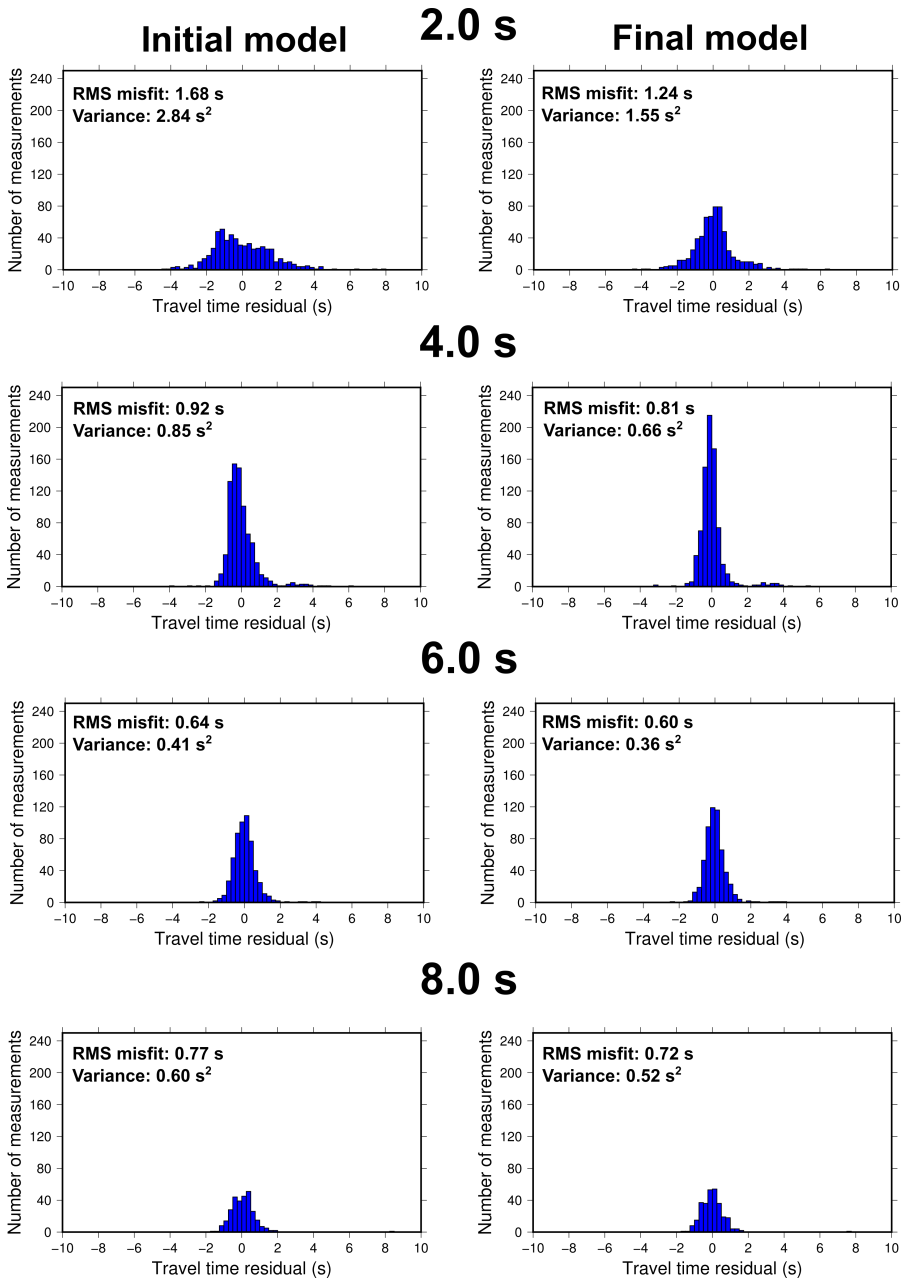

Figure S5. Data misfit of the Rayleigh wave phase velocity tomography at periods 2.0, 4.0, 6.0 and 8.0 seconds. We show the travel time residual in 0.25 s bins, and the number of measurements that fall in each bin. The left hand column shows the misfit of the original, constant velocity inversion, and the right hand column shows the misfit of the final tomography model. Each histogram is labelled with the corresponding root mean square misfit and variance of the travel time residuals.

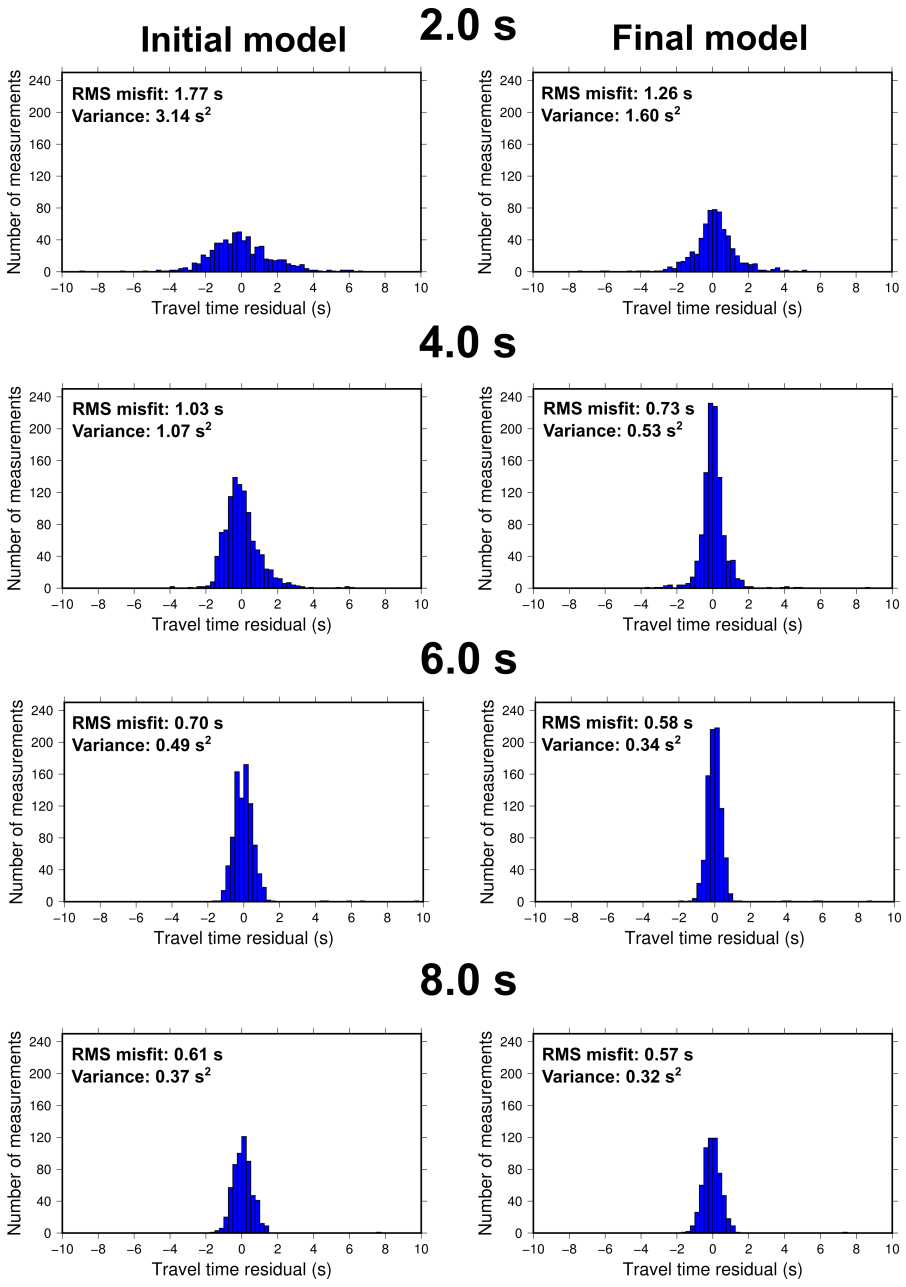

Figure S6. Data misfit of the Love wave phase velocity tomography at periods 2.0, 4.0, 6.0 and 8.0 seconds. We show the travel time residual in 0.25 s bins, and the number of measurements that fall in each bin. The left hand column shows the misfit of the original, constant velocity inversion, and the right hand column shows the misfit of the final tomography model. Each histogram is labelled with the corresponding root mean square misfit and variance of the travel time residuals.

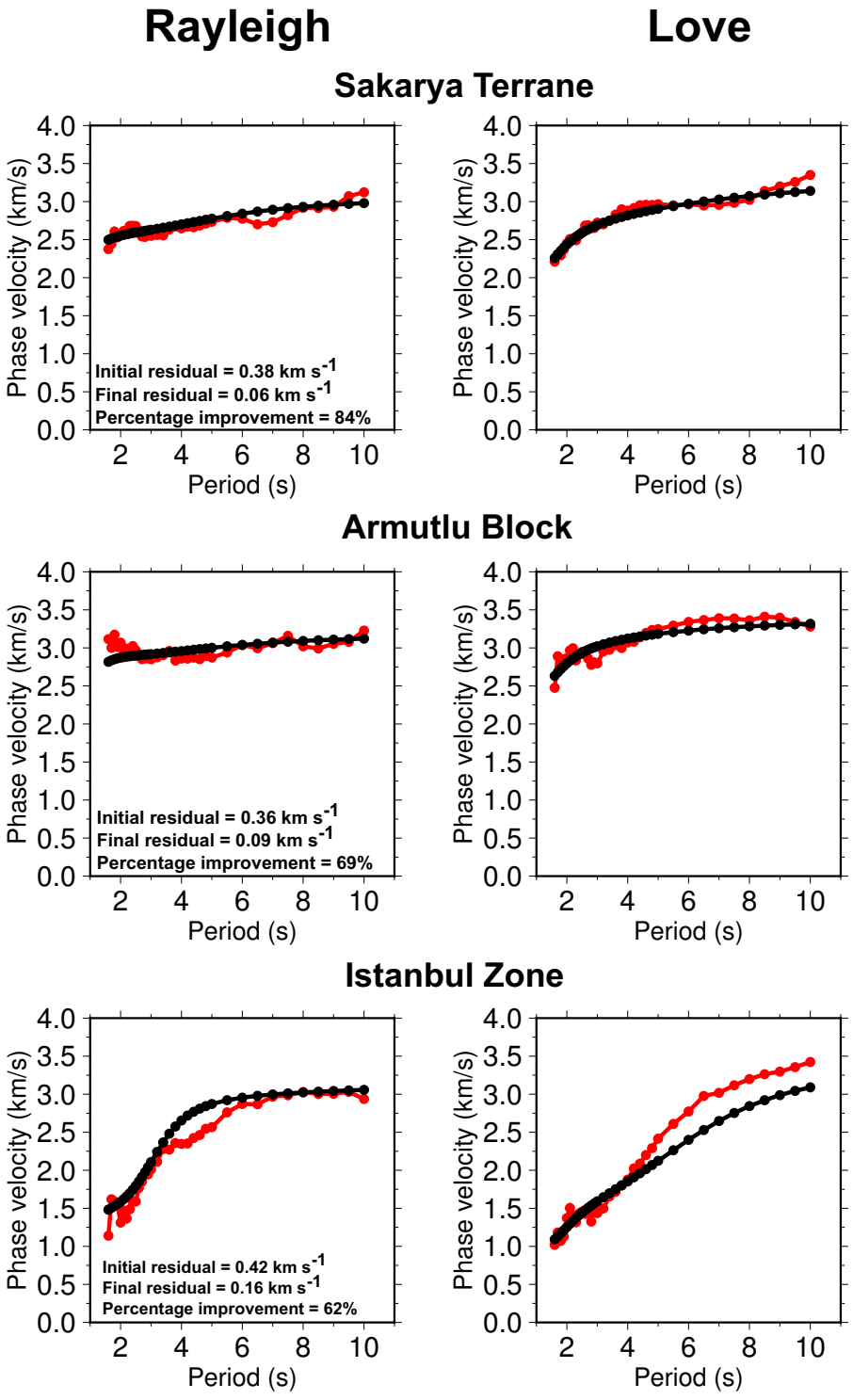

Figure S7. Dispersion misfit of the S-wave velocity inversion at the three nodes shown in Fig. 5 (main text). The fit for Rayleigh wave phase velocities is shown in the left column, Love wave fits are shown on the right. The target dispersion curves from the phase velocity inversion is shown in black, and the red curves show the dispersion calculated from our final S-wave velocity model. The improvement in data fit at each node that results from applying the linearised inversion to the result of the neighbourhood algorithm is indicated on each row, including the final average data residual.

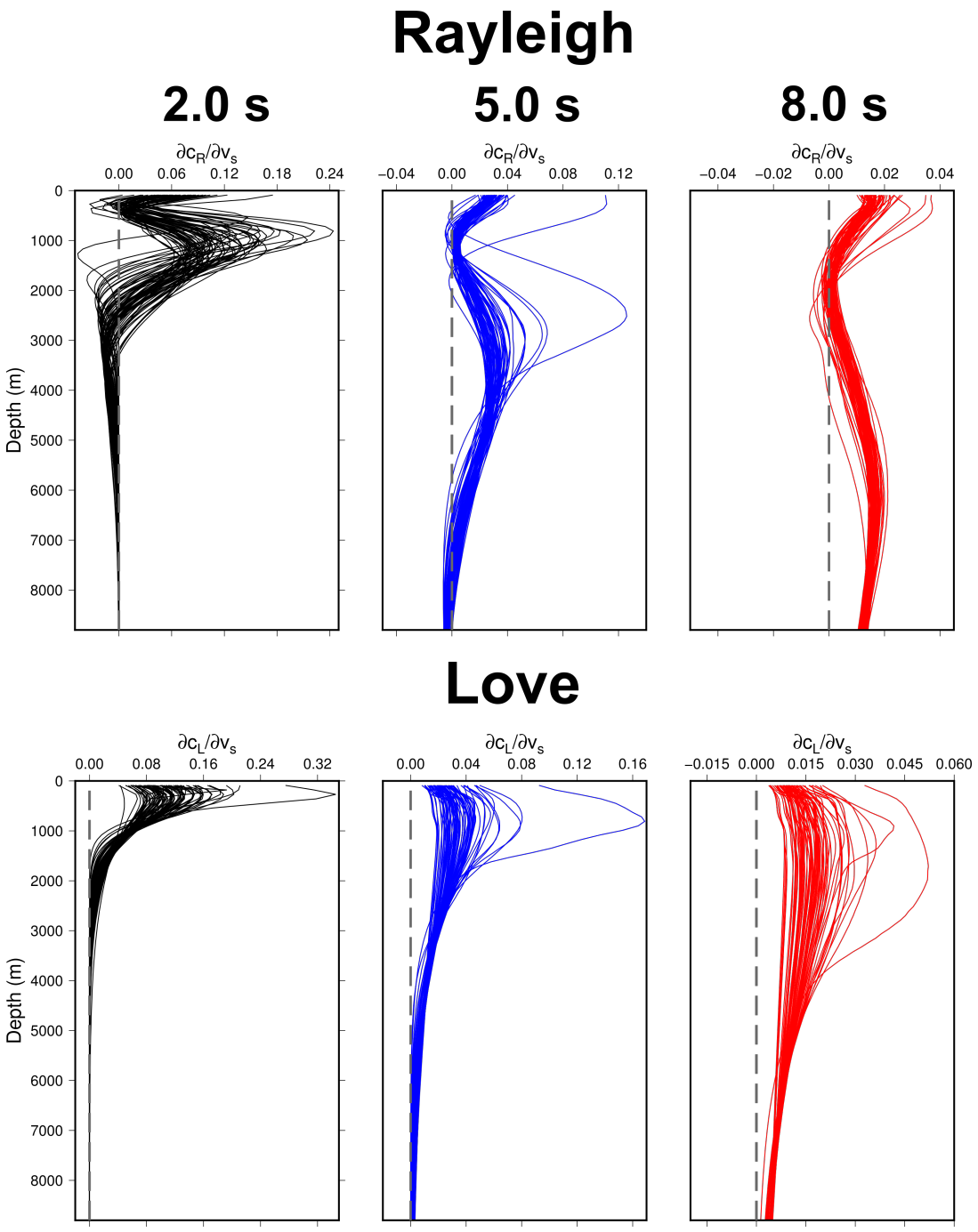

Figure S8. Top: Partial derivatives of Rayleigh wave phase velocity with respect to S-wave velocity at each grid point in our final S-wave velocity model. Bottom: Partial derivatives of Love wave phase velocity with respect to S-wave velocity at each grid point in our final S-wave velocity model. Black lines show sensitivity at 2.0 s period, blue lines 5.0 s period and red lines 8.0 s period.

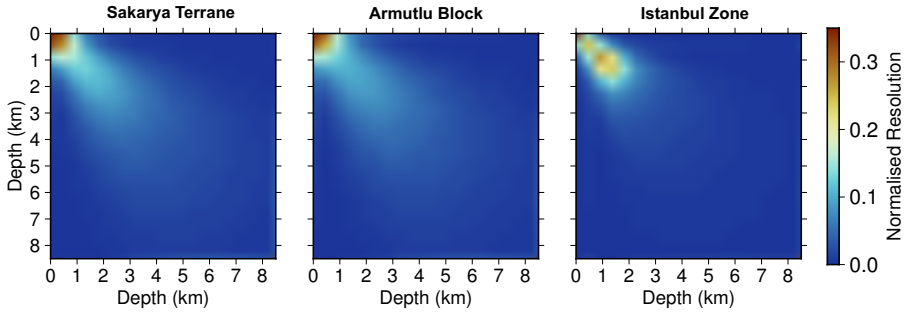

Figure S9. Resolution matrix of the final, linearised S-wave velocity inversion. Red colours indicate high resolution, and blue colours indicate lower resolution. The ideal resolution matrix would consist of the identity matrix - a perfectly diagonal matrix. The further from identity the resolution matrix becomes, the larger the trade offs between different depths in the model.

Text S10. Azimuthal anisotropy of Love wave phase velocities.

Fig. S16 shows the azimuthal variation of the Love wave phase velocities between 0 and 180 degrees from north. The measurements have a higher variance than the Rayleigh wave counterparts, and the dominant fast direction varies between 25 and 40 degrees for the 2θ component. The 4θ component generally has a fast direction between 85 and 120 degrees. The average amplitude of the 2θ component is 0.036 km s^{-1} 1.3%), whilst the 4θ component has an average of 0.025 km s^{-1} (0.9%).

Text S11. Rose diagrams of Rayleigh and Love wave propagation azimuths.

Figs. S17 and S18 shows the azimuthal distribution of ray coverage for both Rayleigh and Love waves. The azimuthal distribution of ray coverage shows a strong bias to north-south oriented paths in both the Rayleigh and Love waves. The azimuthal distribution could be indicative of the dominant direction of noise propagation at the DANA network (oriented towards the Black Sea and Mediterranean Sea), but is most likely the result of the rectangular array shape, and subsequent better sampling of north-south paths after short paths have been excluded. There is evidence of slight heterogeneity between the Rayleigh and Love wave azimuthal distributions. Rayleigh waves show a slight bias towards NNW - SSW oriented paths, whilst Love waves are more clustered along NNE - SSE ray paths. This could be indicative of a difference in noise source distribution for these two wave types. The fact that less measurements are available at 2.0 s period than at higher periods can be explained by the generally noisier measurements made at short period, for reasons such as higher structural heterogeneity, and the appearance of higher mode surface waves.

Text S11. Description of the final S-wave velocity model file.

The final S-wave velocity model is included as a separate file. This file is an ASCII plain text document and is organized with each row representing: Longitude, Latitude, Depth, S-wave velocity. Each row represents a different node in our final model.

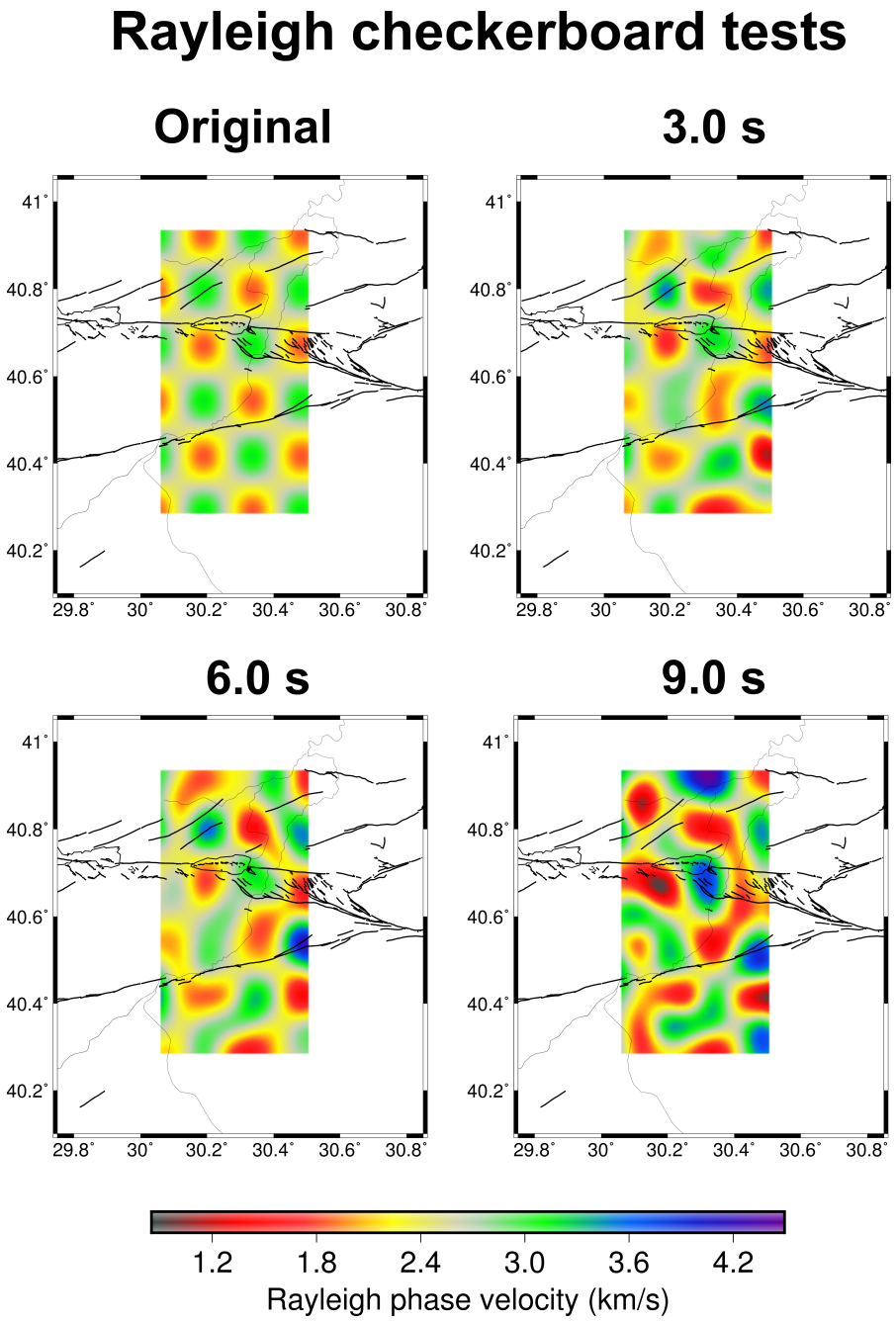

Figure S10. Checkerboard tests for the Rayleigh wave phase velocity tomography between 3.0 s and 9.0 s. The top left panel shows the original checkerboard that we attempt to retrieve using a noisy (Text S9.) synthetic data set with our ray path distribution at each period. Thick black lines represent the locations of the mapped faults. The thin black line represents the Sakarya River.

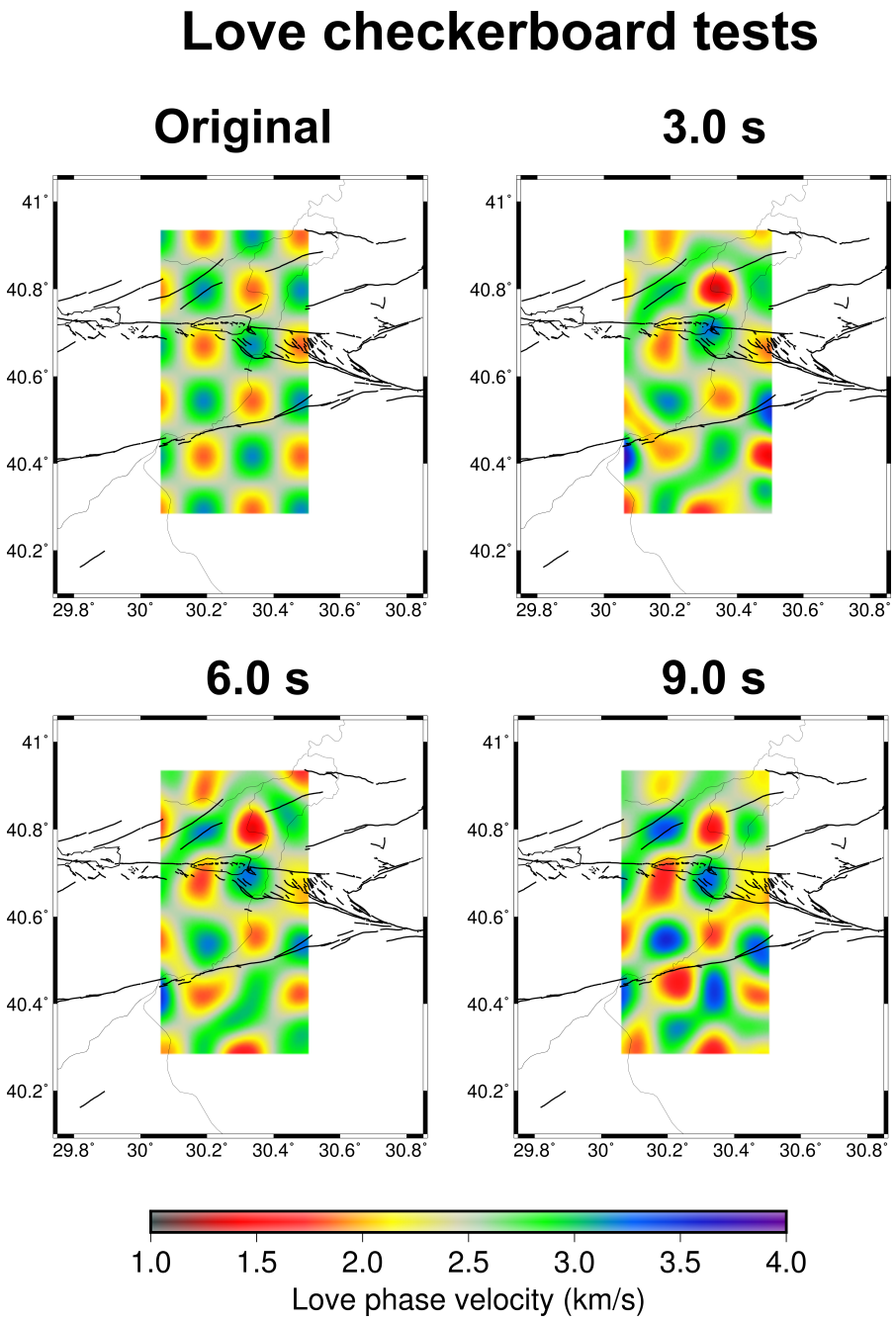

Figure S11. Checkerboard tests for the Love wave phase velocity tomography between 3.0 s and 9.0 s. The top left panel shows the original checkerboard that we attempt to retrieve using a noisy (Text S8.) synthetic data set with our ray path distribution at each period. Thick black lines represent the locations of the mapped faults. The thin black line represents the Sakarya River.

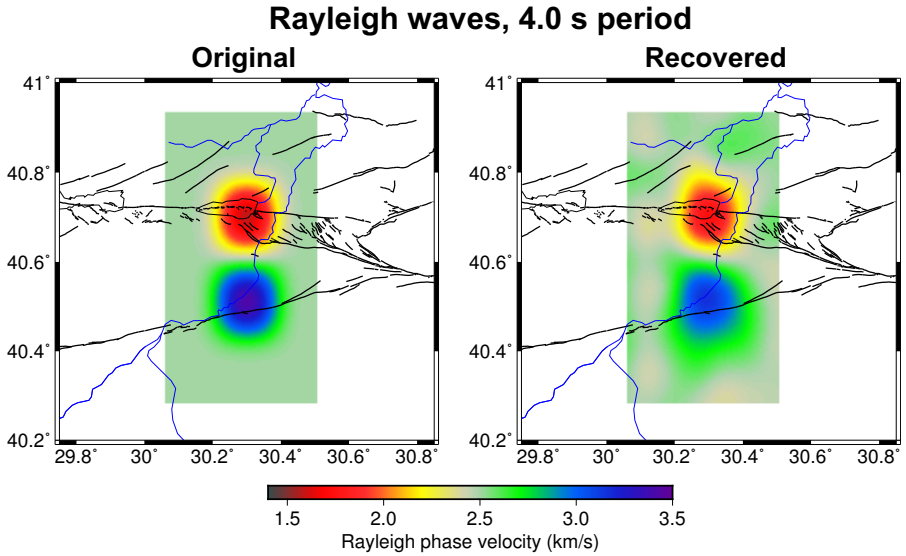

Figure S12. Spike test for the Rayleigh wave velocity at 4.0 s period. The left panel shows the original spike pattern that we attempt to retrieve using a noisy (Text S8.) synthetic data set with our ray path distribution. Thick black lines represent the locations of the mapped faults. The thin black line represents the Sakarya River.

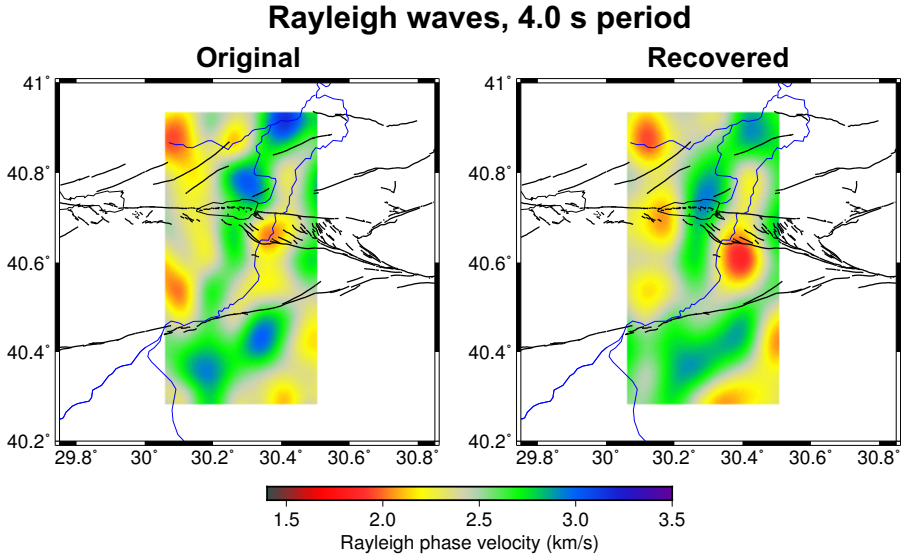

Figure S13. Random model test for the Rayleigh wave velocity at 4.0 s period. The left panel shows the original random pattern that we attempt to retrieve using a noisy (Text S8.) synthetic data set with our ray path distribution. Thick black lines represent the locations of the mapped faults. The thin black line represents the Sakarya River.

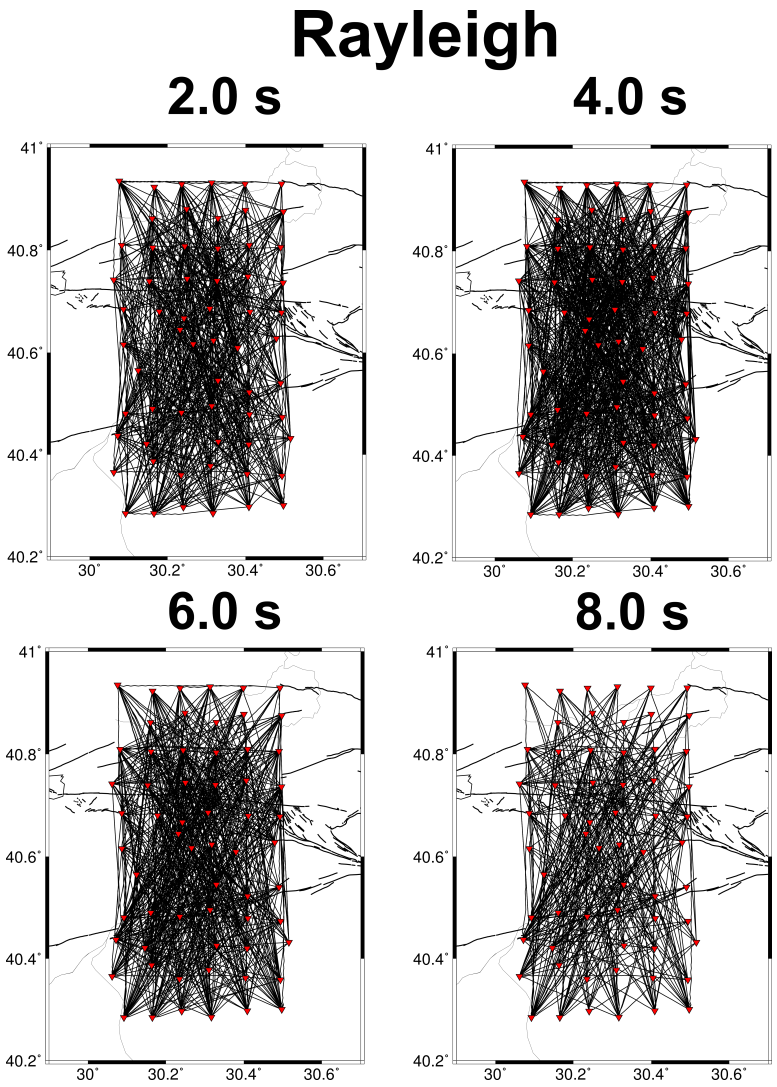

Figure S14. Ray path distribution for the Rayleigh wave phase velocity tomography between 2.0 s and 8.0 s. Red triangles show stations of the DANA network. The black lines connecting them are the ray paths. Thick black lines represent the locations of the mapped faults. The thin black line represents the Sakarya River.

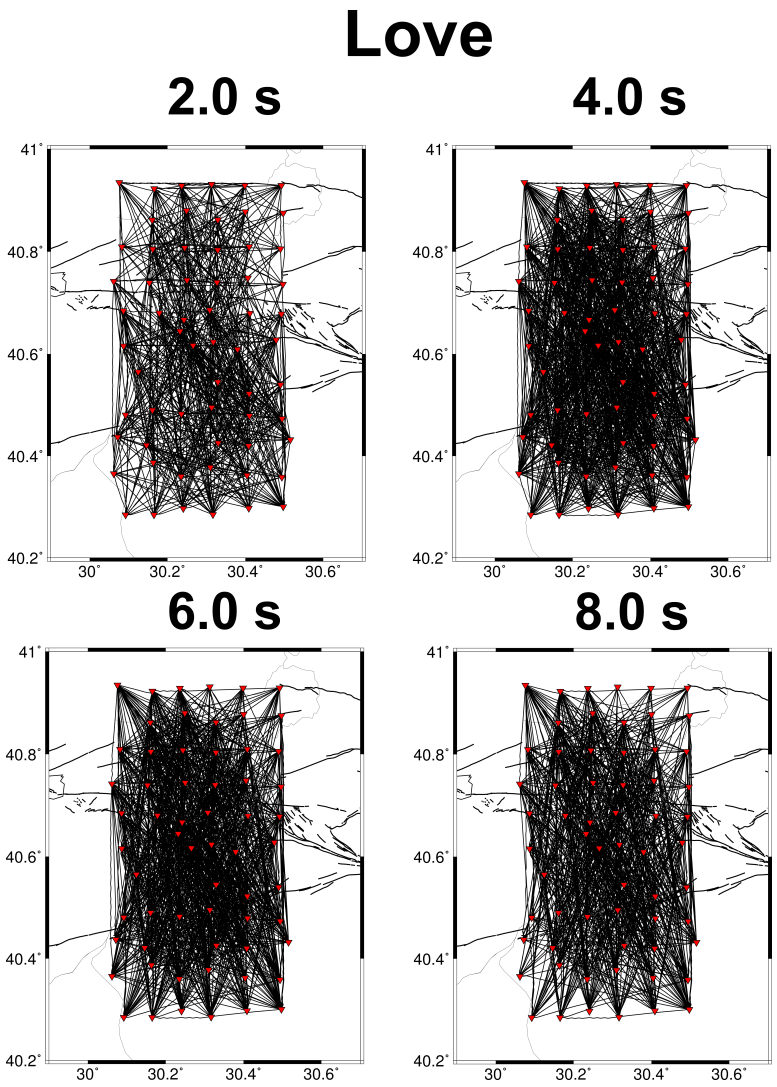

Figure S15. Ray path distribution for the Love wave phase velocity tomography between 2.0 s and 8.0 s. Red triangles show stations of the DANA network. The black lines connecting them are the ray paths. Thick black lines represent the locations of the mapped faults. The thin black line represents the Sakarya River.

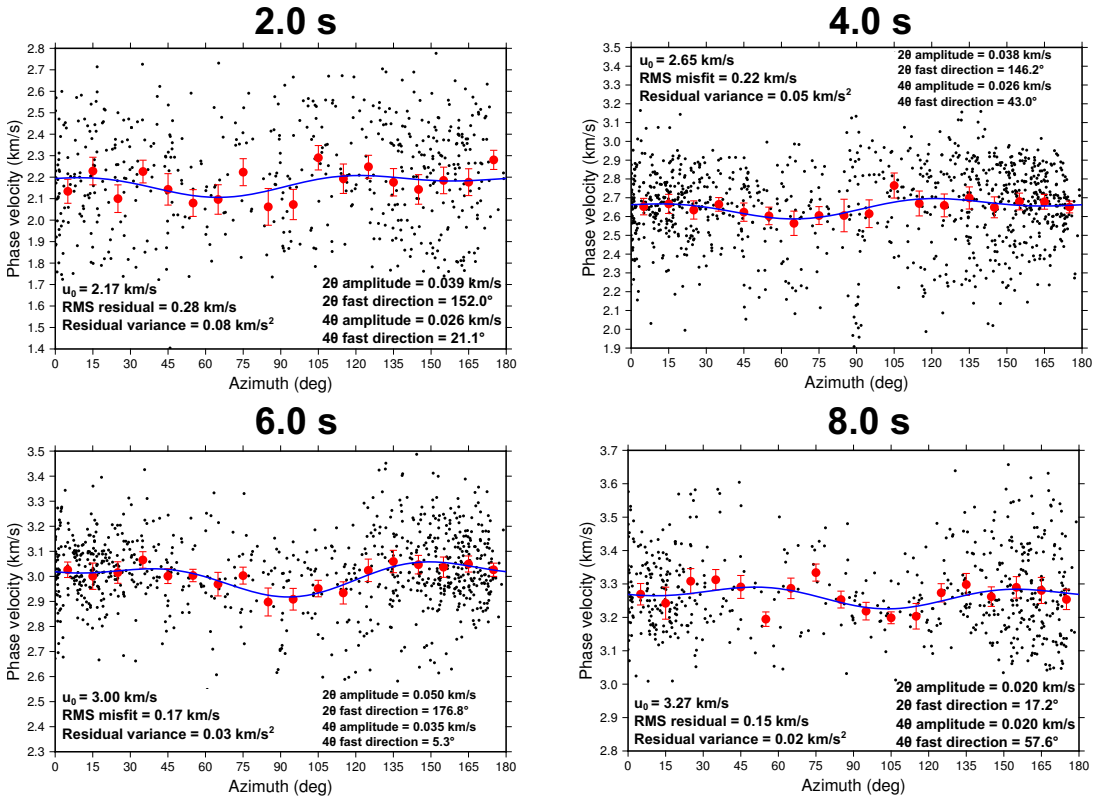

Figure S16. Azimuthal variation of Love wave phase velocities with propagation azimuth (from north). Black dots indicate the raw phase velocity measurements, large red dots show the average of the phase velocities within 5 degree azimuth bins, and the corresponding standard error of the mean for the bin. The blue line is the curve (eq. 3) that best fits the raw data (black dots). u_0 is the average (isotropic) phase velocity. We show the root mean square misfit of the blue curve to the phase velocity measurements, as well as the variance of the residuals. We indicate the 2θ and 4θ amplitudes and fast directions that correspond to the blue curve. The azimuthal distribution of ray paths used in this analysis is shown i supplementary Fig. S15.

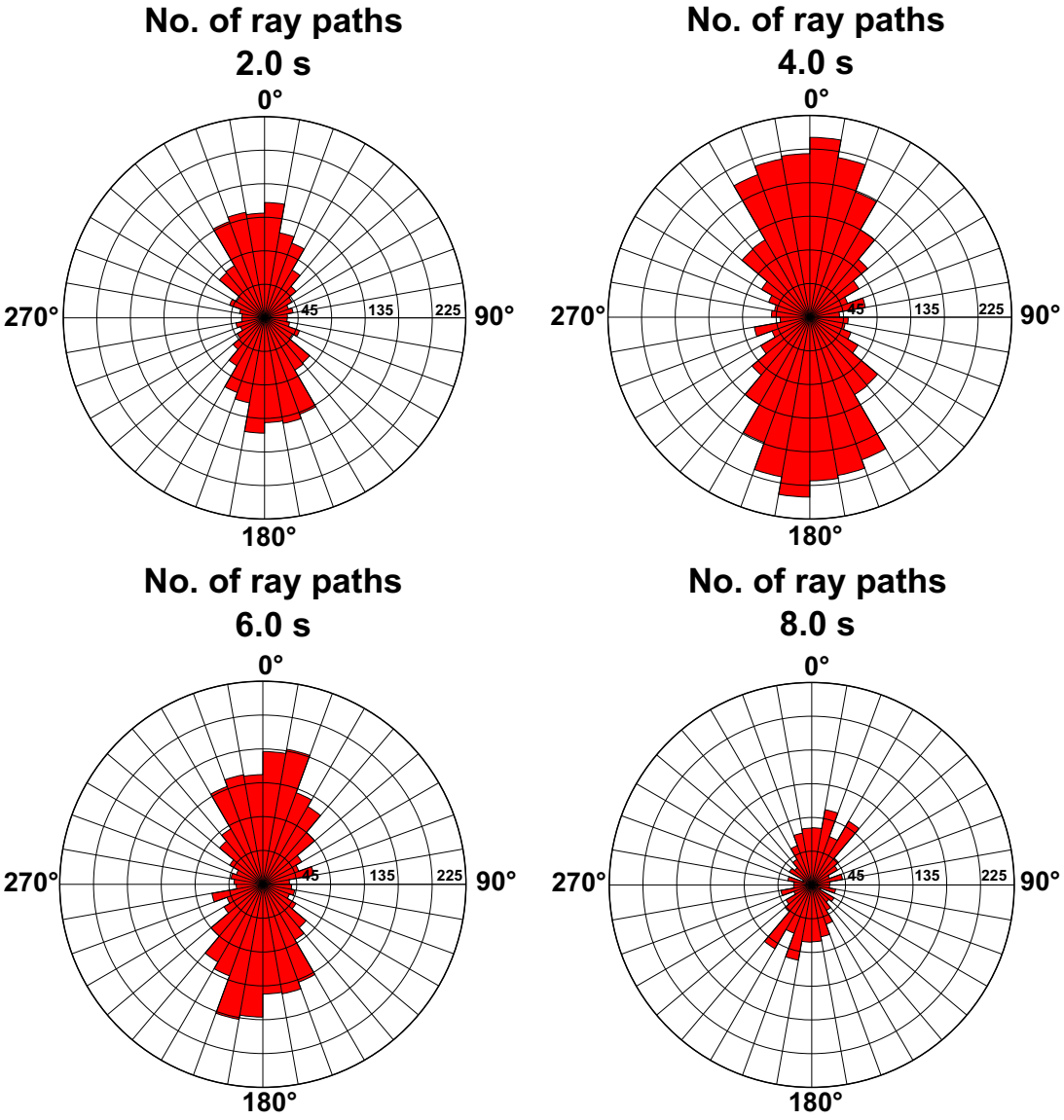

Figure S17. Azimuthal distribution of Rayleigh wave ray coverage at 2 s, 4 s, 6 s and 8 s. The azimuth from north is indicated on the outside of the rose diagram. The data are split into 10 degree azimuth bins. The x-axis indicates the number of rays in the given azimuth bin.

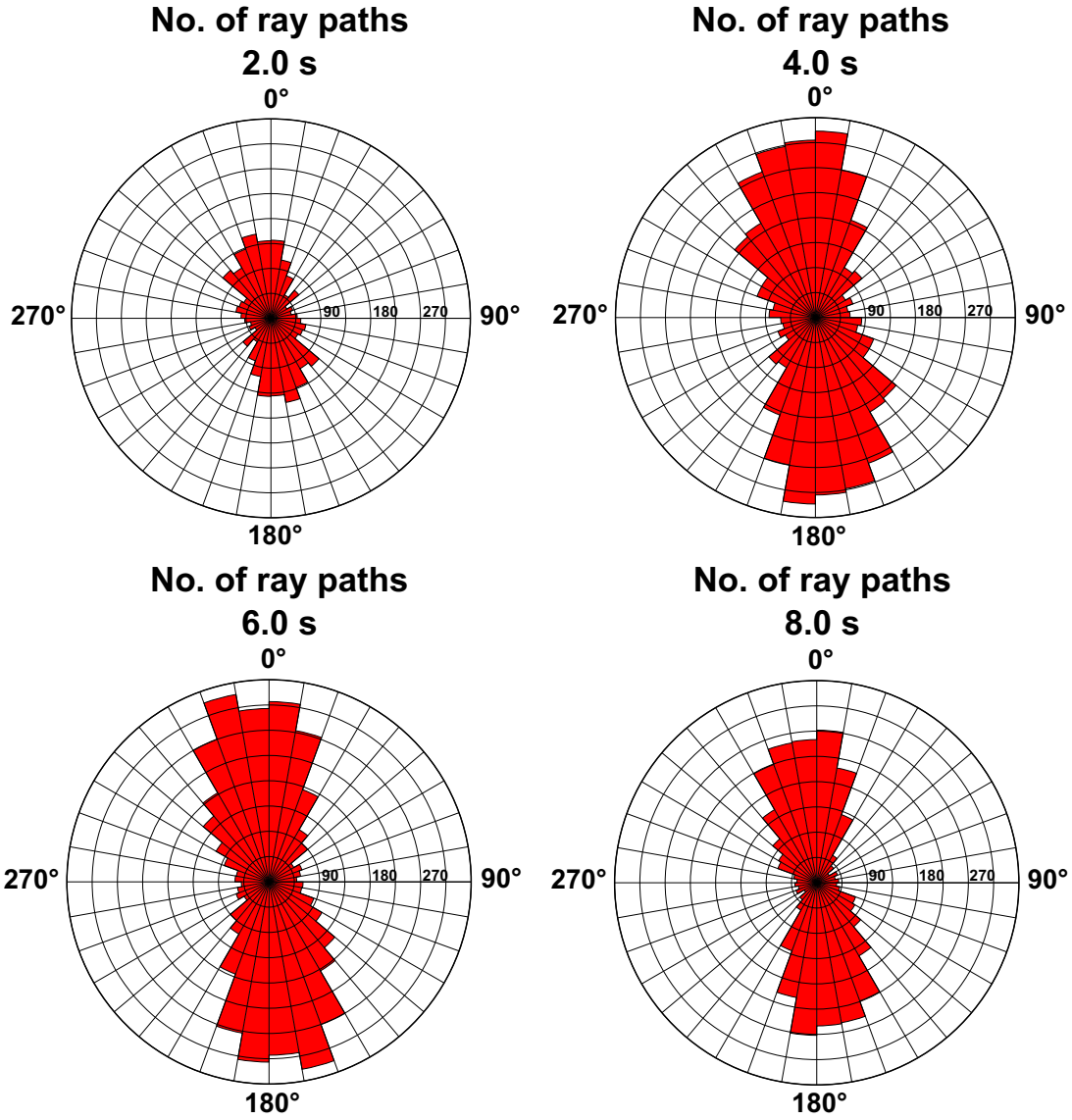

Figure S18. Azimuthal distribution of Love wave ray coverage at 2 s, 4 s, 6 s and 8 s. The azimuth from north is indicated on the outside of the rose diagram. The data are split into 10 degree azimuth bins. The x-axis indicates the number of rays in the given azimuth bin.